

Fe-vacancy ordering in superconducting $K_{1-x}Fe_{2-y}Se_2$: first-principles calculations and Monte Carlo simulations

This content has been downloaded from IOPscience. Please scroll down to see the full text.

2015 Supercond. Sci. Technol. 28 095004

(<http://iopscience.iop.org/0953-2048/28/9/095004>)

View [the table of contents for this issue](#), or go to the [journal homepage](#) for more

Download details:

IP Address: 202.117.31.202

This content was downloaded on 24/09/2015 at 03:33

Please note that [terms and conditions apply](#).

Fe-vacancy ordering in superconducting $K_{1-x}Fe_{2-y}Se_2$: first-principles calculations and Monte Carlo simulations

Yong Fang¹, Yuan-Yen Tai², Junkai Deng¹, Chao Wu^{1,3}, Xiangdong Ding¹, Jun Sun¹ and Ekhard K H Salje^{1,4}

¹ State Key Laboratory for Mechanical Behavior of Materials, Xi'an Jiaotong University, Xi'an 710049, People's Republic of China

² Theoretical division, Los Alamos National Laboratory, Los Alamos, New Mexico 87545, USA

³ Frontier Institute of Science and Technology, Xi'an Jiaotong University, Xi'an 710049, People's Republic of China

⁴ Department of Earth Sciences, University of Cambridge, Cambridge CB2 3EQ, UK

E-mail: dingxd@mail.xjtu.edu.cn and ekhard@esc.cam.ac.uk

Received 4 May 2015

Accepted for publication 17 June 2015

Published 20 July 2015



Abstract

Fe vacancies in the 33 K superconductor $K_{1-x}Fe_{2-y}Se_2$ show ordering schemes that may be correlated with its superconducting properties. First-principles calculations and kinetic Monte Carlo simulations lead to a very simple model for vacancy ordering. Repulsive dipolar interactions between Fe vacancies show three ground states: a $\sqrt{8} \times \sqrt{10}$ rhombus-ordered structure for 12.5% vacancies, a $\sqrt{5} \times \sqrt{5}$ squared lattice for 20% vacancies, and a $\sqrt{5} \times \sqrt{5}$ rhombus-ordered structure for 25% vacancies. Other structural states are derived from these three ground states and may contain additional disordered spatial regions. The repulsive interaction between Fe vacancies arises from enhanced Fe–Se covalent bonds, which differs from the well-known attractive interaction of Fe vacancies in body-centered cubic Fe.

Keywords: Fe-vacancy ordered structure, DFT calculations, MC phase diagram, $K_{1-x}Fe_{2-y}Se_2$

(Some figures may appear in colour only in the online journal)

1. Introduction

Superconductivity with $T_c \sim 33$ K has been observed in $K_{0.8}Fe_{1.7}Se_2$, which inspired a wider interest in Fe-based superconductors [1]. KFe_2Se_2 is a 122-type layered structure with vacancies in the Fe layers. Experimental and theoretical studies have focused on the relationships between superconductivity, structural (vacancy concentration) change, and magnetic order in $K_{1-x}Fe_{2-y}Se_2$ [2–6]. A complex pattern of Fe-vacancy ordering was found:

- (1) A $\sqrt{5} \times \sqrt{5}$ (in units of the nearest Fe–Fe bonds) square-ordered structure of Fe vacancies was observed by transmission electron microscopy (TEM) study of

$K_{0.8}Fe_{1.6}Se_2$ [2, 7–9] with a Fe-vacancy concentration $V_{Fe} = 20\%$. This well-defined structure was named the ‘245 structure’.

- (2) Coexistence of the 245 structure and a disordered vacancy structure (‘disordered’ refers to the disordered distribution of Fe-vacancy in the Fe layer) was found for $V_{Fe} = 19.5\%$ [10].
- (3) A mixed structure composed of a $\sqrt{8} \times \sqrt{10}$ rhombus-ordered structure and the 245 structure was reported when V_{Fe} ranges from 12.5 to 20% [11].
- (4) A $2 \times \sqrt{5}$ rhombus-ordered structure coexisting of a 245 structure was reported for $V_{Fe} = 21\%$ [10].

Since Fe vacancies experimentally show these ordered structures, one may conclude that some repulsive interaction

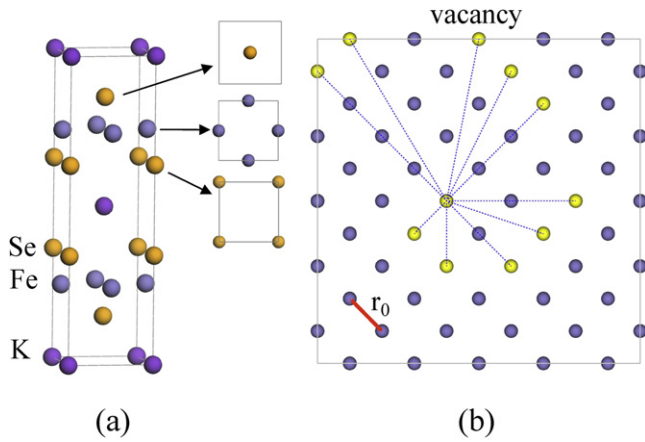


Figure 1. (a) Unit cell of KFe_2Se_2 with K, Fe, and Se atoms shown in purple, blue, and gold, respectively. (b) View along the layer repetition axis of a $5 \times 5 \times 1$ KFe_2Se_2 supercell where only one of the Fe layers is shown. Ten vacancy pairs (indicated by yellow circles) with different distances are indicated by blue dashed lines. The nearest Fe–Fe distance $r_0 = 2.654 \text{ \AA}$ is shown as a red line.

between the vacancies exists [12–18]. This is surprising in view of the known attractive forces between vacancies in body-centered cubic (bcc) Fe. In this paper, we identify by density functional theory (DFT) calculations the origin of the repulsive interaction and derive by Monte Carlo calculations the ground states for a phase diagram of microstructures as a function of the Fe–vacancy concentration. We show that the pair interactions between Fe vacancies are indeed repulsive and follow approximately the dipolar $1/r^3$ spatial dependence.

2. Calculation methods

2.1. DFT calculations

DFT calculations of the interaction between Fe vacancies in $\text{KFe}_{2-y}\text{Se}_2$ were performed using the Atomistix ToolKit (ATK) software package [19]. Figure 1(a) shows the computational model of the KFe_2Se_2 unit cell. It contains 10 atoms and has a layered structure along the c -direction. The optimized lattice constants are $a = b = 3.754 \text{ \AA}$, $c = 13.739 \text{ \AA}$. In the Fe layers, each Fe atom has four nearest Fe neighbors at a distance of 2.654 \AA (denoted as r_0 , shown as the red line in figure 1(b)), and four nearest Se neighbors. Two Se atoms are on the upper Se layer, and the other two Se atoms are on the lower Se layer. We use a $5 \times 5 \times 1$ supercell (250-atom structure) including Fe–vacancy pairs with a given vacancy–vacancy distance (denoted by r_i , where $i = 1 \sim 10$), and relax the structure to calculate the potential energy of the system, then we can calculate the binding energy of a Fe–Fe vacancy pair with different r_i (where $i = 1 \sim 10$, shown in figure 1(b)). We first assume a full mirror-symmetry between the two Fe layers in the unit cell and use the same vacancy pair distribution in both Fe layers. We neglect the effect of other

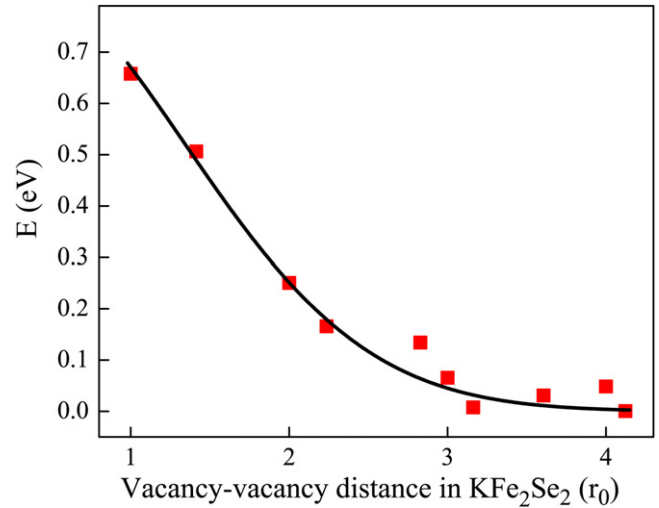


Figure 2. The binding energy of two vacancy pairs (E) as a function of the planar vacancy–vacancy distance. The binding energy is positive and decreases with increasing vacancy distance. The black line is a fitted exponential function.

defects (e.g., K vacancies) in our model, since previous studies have shown that they are distributed randomly in the sample and have little effect on the crystal stability [20, 21]. We do not attempt a full cluster variation analysis and focus entirely on the vacancy pair interaction. In a second step, we investigate the correlations between Fe vacancies in two parallel layers.

Spin-polarized local density approximation (LSDA) with the Perdew–Zunger parameterization was used as the exchange and correlation function [22, 23]. Single zeta plus polarization (SZP) basis set was selected for the electron wave function. A cutoff energy of 75 Hartree and a Monkhorst–Pack k -mesh of $1 \times 1 \times 1$ were used for all calculations of vacancy pairs. Lattice parameters and atomic coordinates were fully relaxed until the maximum force on each atom was less than 0.05 eV \AA^{-1} .

2.2. Monte Carlo simulations

The interaction of Fe vacancies pairs obtained from the DFT calculations were used for Monte Carlo simulations to simulate Fe–vacancy ordering at different Fe–vacancy concentrations. The distribution patterns of Fe vacancies in $\text{KFe}_{2-y}\text{Se}_2$ for $V_{\text{Fe}} = 12.5, 20$ and 25% were derived by kinetic Monte Carlo (KMC) simulations, as previously described in [24, 25]. At a fixed vacancy concentration, Fe vacancies are randomly distributed in a 40×40 structure (in units of $r_0 \times r_0$) with periodic boundary conditions. In order to mimic the annealing process in experiments, step cooling is used in the KMC simulations to avoid the system being trapped in metastable states. All vacancies were allowed to move for each time step.

The energy difference between the different configurations of Fe vacancies, as used for the KMC algorithm, is simplified as pair interactions of Fe vacancies. The relative

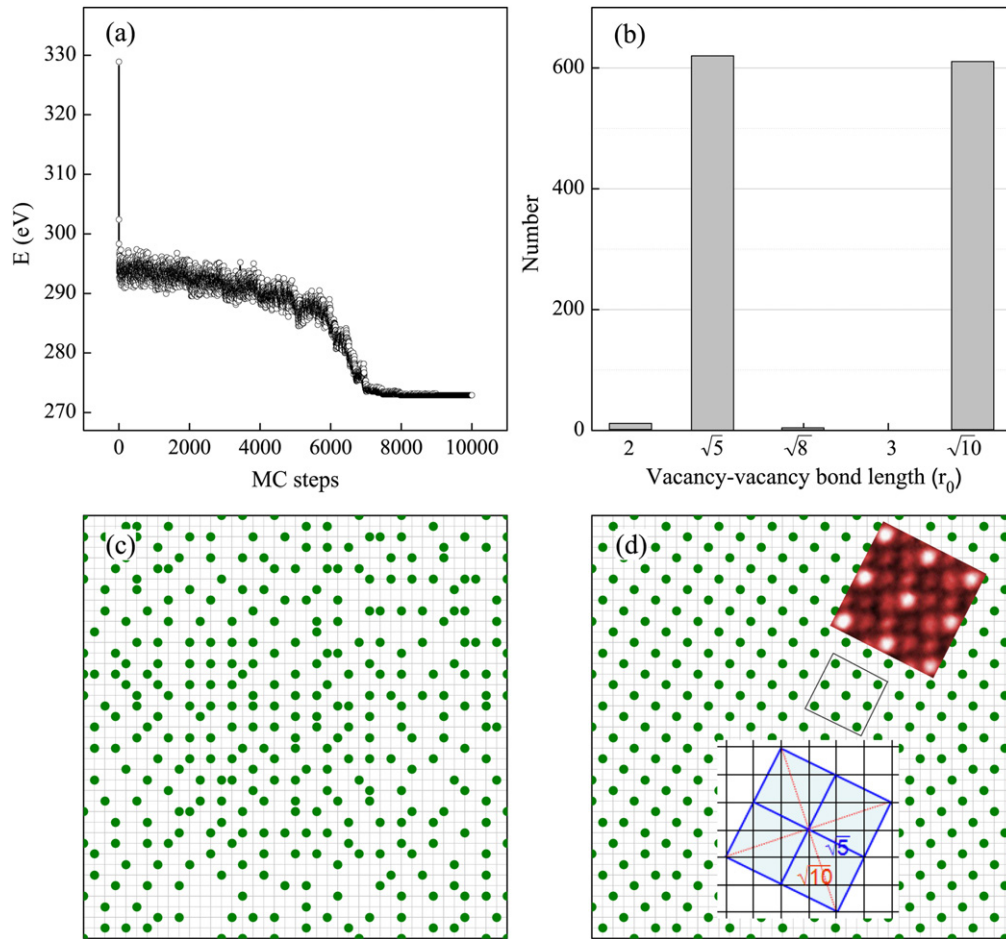


Figure 3. Results of KMC simulations with 20% Fe vacancies. (a) Evolution of the potential energy with MC steps. (b) Number of vacancy–vacancy bonds with different bond lengths. These numbers are averaged over 20 simulations. (c) Initial random distribution of Fe vacancies. (d) Distribution of Fe vacancies after KMC simulations (10000 KMC steps). The stable structure of Fe vacancies is a $\sqrt{5} \times \sqrt{5}$ square-ordered pattern. The inserted figure in (d) shows a corresponding TEM image [7] of the vacancy superstructure. The green circles in (c) and (d) represents Fe vacancies.

energy is $E = \sum_{i=1}^N \sum_{j>i}^N E(r_{ij})$, where N is the total number of vacancies, $E(r_{ij})$ is the binding energy between two vacancies (vacancy i , vacancy j), which is obtained from curve fitting of the binding energy of the vacancy pairs, and r_{ij} is the distance between vacancy i and j . The cutoff interaction distance of the Fe vacancies is set to be $5r_0$.

3. Results

3.1. The interaction of Fe–Fe vacancy pairs in $KFe_{2-y}Se_2$

The binding energy of two Fe–Fe vacancy pairs (E_{2v}^b) is defined as the energy difference between the formation energy of two Fe-vacancy pairs with the distance of r_i (E_{1v}^f) and two times of the formation energies for isolated Fe-vacancy pair (E_{1v}^f), which is written as $E_{2v}^b = E_{2v}^f - 2E_{1v}^f$, where $E_{2v}^b > 0$ indicates a repulsive potential between two vacancies.

The results of the DFT calculations are shown in figure 2 (red squares). In order to derive a smooth version of the

interaction potential we fit the data points and find that the decrease of the binding energy with increasing distance follows the typical dipole–dipole interaction $1/r^3$ for $r > 2r_0$. Almost no interaction was found for $r > 4r_0$. An empirical fit of the data is shown as a black line $E = \exp(-0.16 + 0.13r_0 - 0.37r_0^2)$. This expression is used as empirical potential for vacancy–vacancy pairwise interaction in the MC simulations. This curve is very close to the $1/r^3$ dependence of dipolar interactions. Identical results were found when E is determined numerically for each distance (red points in figure 2) and used as interaction parameters for the MC simulations.

3.2. Fe-vacancy ordering at 20% vacancy concentration

Figure 3(a) shows that the convergence of the potential energy for 20% vacancy concentration as a function of the number of MC steps. Sufficient convergence was reached after 10000 MC steps. The averaged vacancy–vacancy distance distribution is shown in figure 3(b). It shows that the number of bond with $\sqrt{5} r_0$ is almost the same as the number

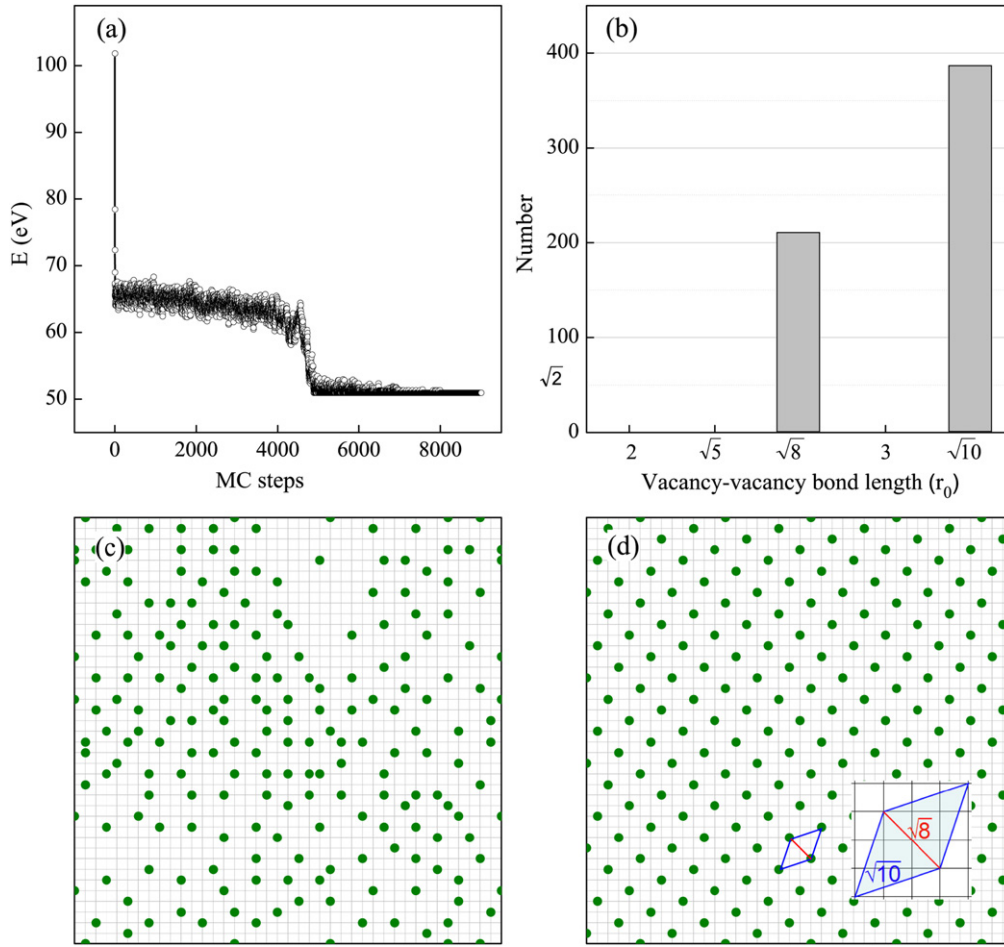


Figure 4. KMC simulation with 12.5% Fe vacancies. (a) Evolution of potential energy of the system with MC steps. (b) Number of vacancy-vacancy bonds with different bond lengths. These numbers are averaged over 20 simulations. (c) Initial random distribution of Fe vacancies. (d) Distribution of Fe vacancies after KMC simulations (9000 KMC steps). The unit structure of Fe vacancies is a $\sqrt{8} \times \sqrt{10}$ rhombus-ordered structure, as shown in the insert in (d). The green circles in (c) and (d) represent Fe vacancies.

of bound with $\sqrt{10} r_0$, indicating an ordered square vacancy structure, shown in figure 3(d).

Figures 3(c) and (d) show the corresponding configuration of Fe vacancies before and after KMC calculation. The initial random distribution of Fe vacancies (figure 3(c)) transform rapidly into the ordered pattern in figure 3(d). This pattern presents the $\sqrt{5} \times \sqrt{5}$ square structure in agreement with experimental results shown in the inset of figure 3(d) [2, 7–9].

3.3. Fe-vacancy ordering at 12.5 and 25% vacancy concentrations

Vacancy ordering equally occurs for other defect concentrations. Figure 4 shows the MC results for 12.5% vacancy concentration. Sufficient convergence was reached after 9000 MC steps (figure 4(a)) when the randomly distributed Fe vacancies of the initial state (figure 4(c)) changed into a $\sqrt{8} \times \sqrt{10}$ rhombus-ordered structure (figure 4(d)). The statistical distribution of the bonding lengths of Fe-vacancy pairs (figure 4(b)) shows that all bond length are either $\sqrt{8} r_0$ or $\sqrt{10} r_0$; and the number of bound

with $\sqrt{10} r_0$ is about two times of the number of bound with $\sqrt{8} r_0$, which characterizes the rhombus-ordered defect structure.

Figure 5 shows the KMC results for 25% concentration. The system reaches an equilibrium state after 15000 MC steps (figure 5(a)), when the randomly distributed Fe vacancies at the initial state (figure 5(c)) change to a $2 \times \sqrt{5}$ rhombus-ordered structure (figure 5(d)). The statistics of the bonding lengths of Fe vacancies (figure 5(b)) show a majority of bond lengths at $2 r_0$ and $\sqrt{5} r_0$ as expected for the $2 \times \sqrt{5}$ structure, while a small proportion of other bond lengths indicates remaining structural disorder.

In order to check the validity of the pair potential for the above MC calculations, we recalculated the total system energy for both square-ordering (2×2 for $V_{\text{Fe}} = 25\%$; $\sqrt{8} \times \sqrt{8}$ for $V_{\text{Fe}} = 12.5\%$) and rhombus-ordering structures ($2 \times \sqrt{5}$ for $V_{\text{Fe}} = 25\%$; $\sqrt{8} \times \sqrt{10}$ for $V_{\text{Fe}} = 12.5\%$) by DFT and found the total energy of the rhombus-ordering scheme is always lower than that of the square-ordering scheme. The rhombus orderings scheme hence represents the ground state of the vacancy ordering structures.

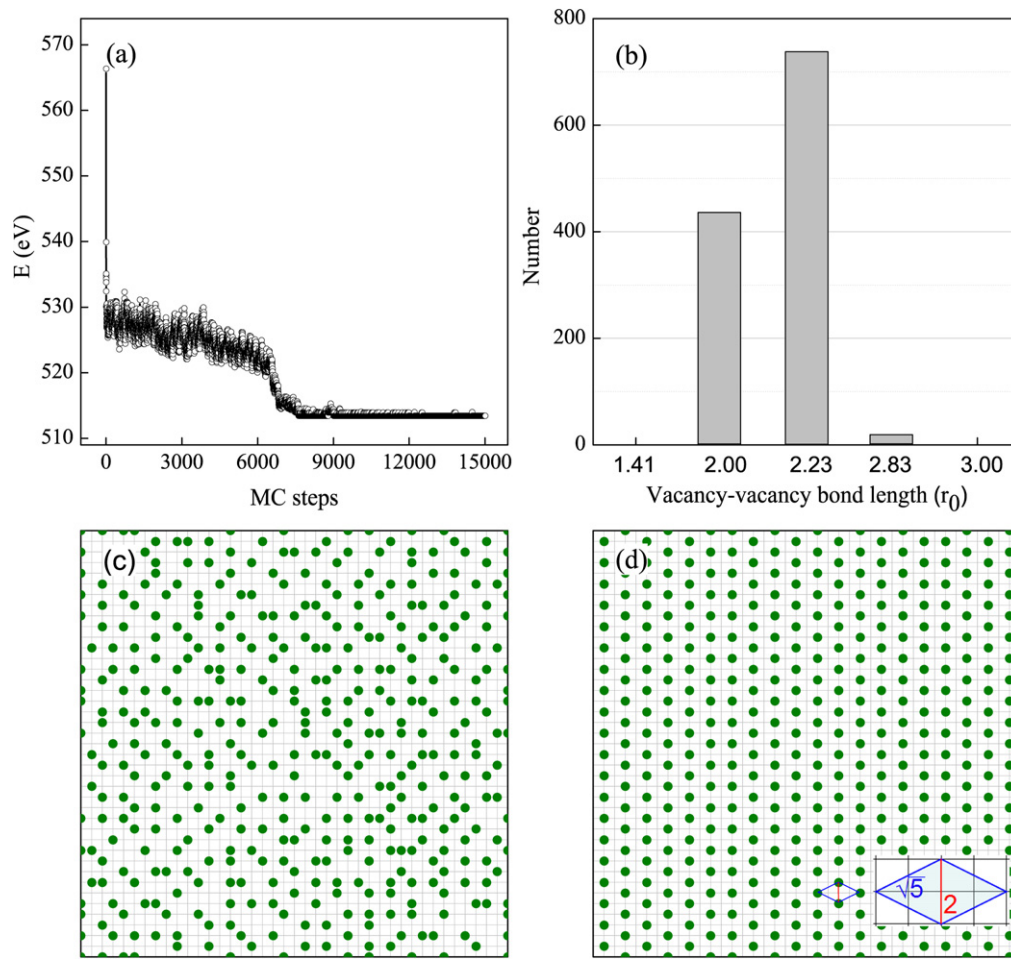


Figure 5. KMC simulation with 25% Fe-vacancy concentration. (a) Evolution of potential energy of the system with MC steps. (b) Number of vacancy–vacancy bonds with different bond lengths. These numbers are averaged over 20 simulations. (c) Initial random distribution of Fe vacancies. (d) Distribution of Fe vacancies after KMC simulations (15000 KMC steps). The unit structure of Fe vacancies is a $2 \times \sqrt{5}$ rhombus-ordered structure, as shown in the inset in (d). The green circles in (c) and (d) represent Fe vacancies.

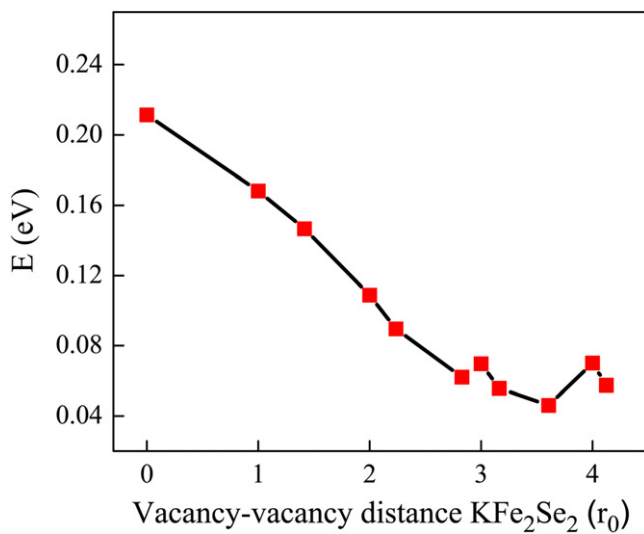


Figure 6. The binding energy of two vacancies (E) in parallel Fe layers of KFe_2Se_2 as a function of the vacancy–vacancy distance. The distance is defined by the projections of the two vacancies onto one Fe plane.

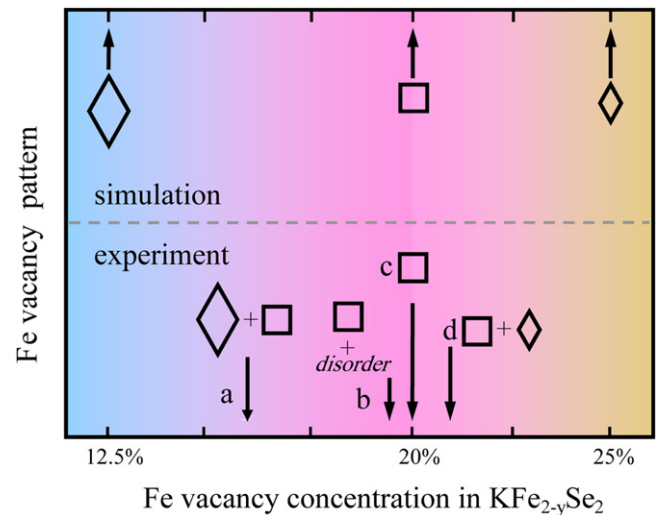


Figure 7. Distribution of Fe-vacancy ordering patterns as function of the vacancy concentration in $\text{KFe}_{2-y}\text{Se}_2$. Three simulation results (top) are compared with four experimental results (bottom) [2, 7–11]. The open squares represent $\sqrt{5} \times \sqrt{5}$ square vacancy patterns, big and small rhombus structures represent the $\sqrt{8} \times \sqrt{10}$ and $2 \times \sqrt{5}$ rhombus vacancy patterns.

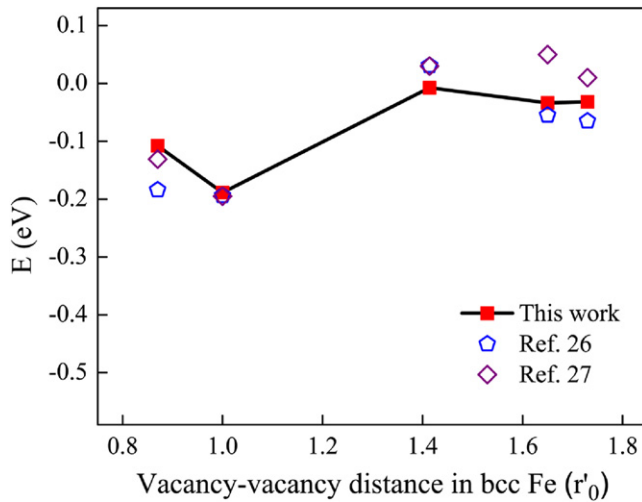


Figure 8. The binding energy of two vacancies (E) as function of vacancy–vacancy distance for bcc Fe. $r_0' = 2.850 \text{ \AA}$ is the lattice constant of bcc Fe at 0 K.

We also calculated the binding energy of two Fe vacancies in two parallel neighboring layers, and the results are shown in figure 6. The binding energy is positive, which means Fe vacancies in parallel layers also interact repulsively so that each layer will register with the next layer to achieve the maximum distance between the vacancies. Since Fe vacancies repel each other both in the Fe layer (figure 2) and between Fe layers, we believe the experimental observed patterns are the statistic results of Fe vacancies distribution under these two repulsive forces.

4. Discussion

We can now construct a tentative ‘phase diagram’ for vacancy ordering and compare the results with experimental observations in figure 7. The results of the model simulations are shown in the upper panel, the square represents the $\sqrt{5} \times \sqrt{5}$ square-ordered pattern at 20% concentration, the big and small rhombuses represent the $\sqrt{8} \times \sqrt{10}$ and $2 \times \sqrt{5}$ patterns at concentrations of 12.5 and 25%. Four experimental patterns are plotted in the lower panel of figure 7 with concentrations of ca. 12.5~20% [11], 19.5% [10], 20% [2, 7–9], and 21% [10], respectively. There is good agreement between the two approaches. First, at $V_{\text{Fe}}=20\%$, the calculated Fe-vacancy ordering agrees with the experiment. Second, at $V_{\text{Fe}}=19.5\%$, the observed microstructure is a coexistence of a $\sqrt{5} \times \sqrt{5}$ square-ordered phase and disordered regions. This experimental result may represent a non-equilibrium state where the $\sqrt{8} \times \sqrt{10}$ rhombus-ordered phase has not yet nucleated. Third, the expected phase mixtures occur at $V_{\text{Fe}}=12.5\%$ and $V_{\text{Fe}}=21\%$.

The repulsive nature of the pairwise Fe-vacancy interaction is in stark contrast to the well-known attractive interaction of vacancies in bcc Fe [26, 27]. To check the validity of our approach we recalculate the inter-vacancy interactions

in bcc Fe. The optimized lattice constant of bcc Fe crystal structure at 0 K is 2.850 \AA (denoted as r_0'). Based on five $5 \times 5 \times 5$ supercells with one vacancy pair, the calculated binding energy of two vacancies as a function of the vacancy–vacancy distance is shown in figure 8. This energy is lower for small distances corresponding to first and second nearest neighbor distances in bcc Fe. When the distance is larger than the fourth nearest neighbor, the energy remains nearly constant. This result is in agreement with previous studies [26, 27], and shows that the interaction of vacancies in bcc Fe crystal is indeed attractive in contrast to that in KFe_2Se_2 .

Following the analysis in [14, 28], we know that the binding energy between vacancies is mainly determined by the electronic properties intrinsic to each metallic species. In the present studies, bcc Fe is a pure metallic system, whereas Fe atoms in KFe_2Se_2 have both metallic and covalent characteristics (metallic Fe–Fe bonds along two-dimensional Fe layer, and covalent Fe–Se bonds between the Fe–Se layer). The different interaction behavior of Fe vacancies may then arise from the different bonding environments around the existed vacancy. For this purpose, we calculated the charge density differences of these two systems. The charge density difference is $\Delta\rho = \rho_{\text{(total)}} - \sum\rho_{(i)}$, where $\rho_{\text{(total)}}$ is the self-consistent total charge density and $\sum\rho_{(i)}$ contains the sum over the charge density of all localized atoms.

Figure 9(a) shows the top view of two layers of 250 atom bcc Fe structure, and one selected area is depicted by a gray square. In this area, atoms $\text{Fe}_1 \sim \text{Fe}_4$ are located in the same Fe layer, while atom Fe_0 is located in another Fe layer. The influence of vacancy on the charge density differences of the selected area are shown in figures 9(b) and (c), respectively. When a Fe-vacancy replaces the atom Fe_1 , its nearest neighbor (Fe_0 , with the distance of $0.87 r_0'$, where r_0' is the lattice constant of bcc Fe at 0 K) and next nearest neighbor (Fe_2 and Fe_3) show strong variations of their charge redistributions, while not much changes for the other atoms. This redistribution of charge density may weaken the Fe–Fe bonds of its next nearest neighbor. As a result, the vacancy formation energies at the positions of Fe_1 and Fe_2 (Fe_3) become lower, and Fe vacancies prefer to attract each other.

For the case of KFe_2Se_2 , every Fe atom has four metallic Fe–Fe bonds along the Fe layer and four covalent Fe–Se bonds toward the adjacent layers (as shown in figure 10). When atom Fe_1 is replaced by a vacancy, the metallic Fe–Fe bond among the nearest Fe neighbors (e.g., $\text{Fe}_1\text{--Fe}_2$, or $\text{Fe}_1\text{--Fe}_3$, in figure 10(b)) is broken (shown in figure 10(c)), while the covalent bond among the vacancy and second nearest neighbor (e.g., $\text{Fe}_2\text{--Se}_0$) is strongly enhanced. Such an enhanced directional covalent bond could stabilize the nearest Fe atoms (Fe_2 and Fe_3) [28]. As a result, another new Fe-vacancy will not prefer to stay at the next nearest neighbor of the pre-existing vacancy, thus leading to the repulsive forces between vacancy pairs.

In summary, vacancy ordering in bcc Fe and KFe_2Se_2 is very different: while defect clustering and attractive forces dominate bcc Fe, repulsive forces lead to the formation of ordered defect structures in $\text{KFe}_{2-y}\text{Se}_2$.

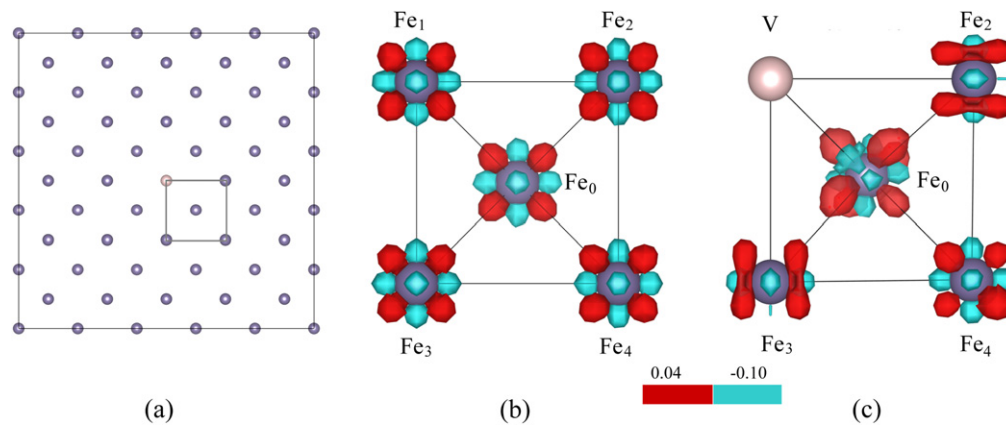


Figure 9. (a) Top view of a $5 \times 5 \times 5$ bcc Fe supercell. The charge density difference maps of the square region in (a) are shown without (b) and with (c) Fe-vacancy. $\text{Fe}_1 \sim \text{Fe}_4$ are located in the upper Fe layer and Fe_0 in the lower Fe layer. Nearest neighbor and next nearest atoms show strong variations of their charge redistributions due to the vacancy while other atoms remain unaffected. The charge density isosurface of the red regions is $0.04 \text{ electrons}/\text{\AA}^3$ and $-0.10 \text{ electrons}/\text{\AA}^3$ in the blue regions.

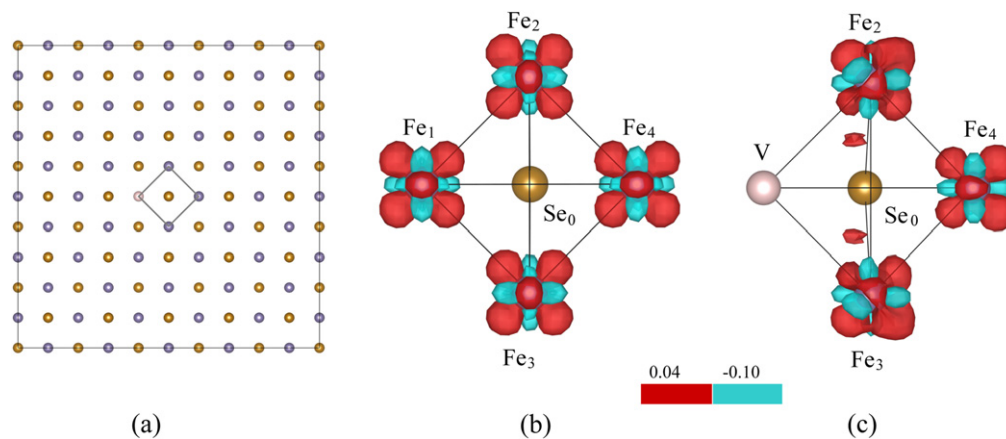


Figure 10. (a) Top view of the $5 \times 5 \times 1$ KFe_2Se_2 supercell showing the Se-Fe-Se layers. The electron density difference maps of the square region in (a) are shown without (b) and with (c) Fe-vacancy. Atoms $\text{Fe}_1 \sim \text{Fe}_4$ are located in the same Fe layer and Se_0 in the adjacent Se layer. The comparison of (b) and (c) shows the charge redistribution by the vacancy. The $\text{Fe}_2\text{-Se}_0$ and $\text{Fe}_3\text{-Se}_0$ bonds are enhanced by the vacancy formation. The isosurface values are the same as that in figure 9.

Acknowledgments

We are grateful to the Natural Science Foundation of China (51171140, 51231008, 51320105014, 51321003, and 51471126), and the Program of Introducing Talents of Discipline to Universities in China project (B06025). EKHS is grateful to EPSRC for funding (Grant No. EP/K009702/1). YYT was supported by the US DOE Contract No. DE-AC52-06NA25396 through the LANL LDRD Program.

References

- [1] Dagotto E 2013 *Rev. Mod. Phys.* **85** 849
- [2] Bao W *et al* 2011 *Chin. Phys. Lett.* **28** 086104
- [3] Wang D M, He J B, Xia T L and Chen G F 2011 *Phys. Rev. B* **83** 132502
- [4] Guo J *et al* 2012 *Phys. Rev. Lett.* **108** 197001
- [5] Wang Z *et al* 2011 *Phys. Rev. B* **83** 140505
- [6] Chen T K *et al* 2014 *Proc. Natl Acad. Sci.* **111** 63
- [7] Song Y J *et al* 2011 *Euro. Phys. Lett.* **95** 37007
- [8] Ye F *et al* 2011 *Phys. Rev. Lett.* **107** 137003
- [9] Kazakov S M *et al* 2011 *Chem. Mater.* **23** 4311
- [10] Zhao J, Cao H B, Bourret-Courchesne E, Lee D H and Birgeneau R J 2012 *Phys. Rev. Lett.* **109** 267003
- [11] Ding X X *et al* 2013 *Nat. Commun.* **4** 1897
- [12] Goncalves-Ferreira L, Redfern S A T, Artacho E, Salje E and Lee W T 2010 *Phys. Rev. B* **81** 024109
- [13] Deng J K *et al* 2010 *Phys. Rev. B* **82** 184101
- [14] Carling K *et al* 2000 *Phys. Rev. Lett.* **85** 3862
- [15] Wigner E 1934 *Phys. Rev.* **46** 1002
- [16] Bonsall L and Maradudin A A 1977 *Phys. Rev. B* **15** 1959
- [17] Tanatar B and Ceperley D M 1989 *Phys. Rev. B* **39** 505
- [18] Rapisarda F and Senatore G 1996 *Aust. J. Phys.* **49** 161
- [19] www.quantumwise.com
- [20] Zhang A M *et al* 2012 *Phys. Rev. B* **86** 134502
- [21] Yan X W, Gao M, Lu Z Y and Xiang T 2011 *Phys. Rev. B* **83** 233205
- [22] Srivastava G P and Weaire D 1987 *Adv. Phys.* **26** 463
- [23] Perdew J P and Zunger A 1981 *Phys. Rev. B* **23** 5048
- [24] Young W M and Elcock E W 1966 *Proc. Phys. Soc.* **89** 735
- [25] Kushima A and Yildiz B 2010 *J. Mater. Chem.* **20** 4809
- [26] Kandaskalov D, Mijoule C and Connetable D 2013 *J. Nucl. Mater.* **441** 168
- [27] Beeler J R and Johnson R A 1967 *Phys. Rev.* **156** 677
- [28] Uesugi T, Kohyama M and Higashi K 2003 *Phys. Rev. B* **68** 184103